



Preparation and electrochemical performance of nanocarbon-isolated nano-sheet silicon lithium-ion battery anode material

Wanzhou Sun¹ · Lu Xu¹ · Aiping Zhu¹

Received: 14 June 2022 / Revised: 31 July 2022 / Accepted: 16 August 2022 / Published online: 23 August 2022
© The Author(s), under exclusive licence to Springer-Verlag GmbH Germany, part of Springer Nature 2022

Abstract

In this paper, nanocarbon-isolated nano-sheet silicon(Si) electrode Si@CNT/C has been developed by pyrolysis of the compound of Si and polyaniline (PANI)/CNT nanocomposite. The results suggest that CNT content in electrode plays a decisive role in the specific capacity, rate capability, and long-term cycle stability of the battery. Si@CNT(M)/C/graphite(G) electrode with high (10.8wt%) CNT content demonstrates the specific capacity of $1201 \text{ mAh}\cdot\text{g}^{-1}$ at $100 \text{ mA}\cdot\text{g}^{-1}$ current density, which is much better than $491 \text{ mAh}\cdot\text{g}^{-1}$ for the Si@CNT(S)/C/G with low (1.3wt%) CNT content. After 500 cycles, the Si@CNT(M)/C/G electrode still remains $700 \text{ mAh}\cdot\text{g}^{-1}$ specific capacity, while the Si@CNT(S)/C/G electrode decreases to $200 \text{ mAh}\cdot\text{g}^{-1}$. This is caused by CNT conductive network in the electrode, which can maintain not only the structural stability of the Si but also the conductivity throughout the cell cycles.

Keywords Silicon carbon anode · Specific surface area · Carbon nanotubes · Electrochemical properties

Introduction

Energy and environment are important themes for the sustainable development of human society. The continuous consumption of coal, oil and natural gas has led people to pay more and more attention to environmental pollution and the consumption of mineral energy. Therefore, lithium rechargeable batteries have received worldwide attention as a clean energy source [1–3]. Lithium-ion batteries (LIBs) are important power sources for portable electronic products, power tools, and electric vehicles. The anode material is a key component of lithium-ion batteries and determines the performance of the entire lithium-ion battery [4]. Most commercial lithium-ion batteries use graphite as the negative electrode and lithium cobalt oxide (LiCoO_2) as the positive electrode. Compared with commercial standards, the theoretical capacity ($372 \text{ mAh}\cdot\text{g}^{-1}$) of graphite is limited [5–7]. The Si active material with ultra-high theoretical capacity ($4200 \text{ mAh}\cdot\text{g}^{-1}$) and abundant natural reserves is considered to be a promising candidate material for the anode of the next generation of LIBs.

However, during the lithiation and extraction process, Si undergoes a large volume change ($> 300\%$), which will produce mechanical strain, lead to electrode powder, electrical contact loss [8–11], resulting in poor electrochemical stability. These problems will lead to the rapid failure of the battery, hindering its practical application. In order to alleviate the above-mentioned problems, various modified silicon-based anodes have been synthesized. Among them, silicon carbon electrode material is considered to have the most application prospect.

Yin et al. [12] reduced the size of Si to nanometer size, the resulting nest-like Si nanospheres still showed a specific capacity of $1095 \text{ mAh}\cdot\text{g}^{-1}$ after 48 cycles at the current density of $2000 \text{ mA}\cdot\text{g}^{-1}$. Lee et al. [13] prepared Si/graphite/carbon composite material, which exhibits a reversible specific capacity of $700 \text{ mAh}\cdot\text{g}^{-1}$, a coulombic efficiency of 86% under $0.2 \text{ mA}\cdot\text{cm}^{-2}$ in the first cycle, and a stable capacity retention. Huang et al. [14] prepared phosphorus doped Si/graphite anode, which exhibits a specific capacity of $883.4 \text{ mAh}\cdot\text{g}^{-1}$ after 200 cycles at the current density of $200 \text{ mA}\cdot\text{g}^{-1}$. Su et al. [15] prepared a spherical Si/graphite@graphene composite material, which exhibits a high initial charge capacity of $820.7 \text{ mAh}\cdot\text{g}^{-1}$ at $50 \text{ mA}\cdot\text{g}^{-1}$, with an initial coulombic efficiency of 78.0%, and still deliver an initial charge capacity of $766.2 \text{ mAh}\cdot\text{g}^{-1}$ at $500 \text{ mA}\cdot\text{g}^{-1}$. Seo et al. [16] forms (Si/

✉ Aiping Zhu
apzhu@yzu.edu.cn

¹ School of Chemistry and Chemical Engineering, Yangzhou University, Jiangsu 225002, People's Republic of China

SiO₂/C)/CNT&Carbon nanofibers anode, its capacity shows 1528 mAh/g for the 1st cycle and 1055 mAh/g for the 50th cycle with 83% capacity retention, caused by high electrical conductivity and low charge transfer resistance. However, much of the above preparation process of Si/C anode is complicated and difficult to industrialize [17].

In order to solve the above problems of low conductivity, large volume change and the preparation process difficult to be industrialized of Si/C anode, herein, the nanocomposites with CNT uniformly distributed in Si/C was constructed. The nanocarbon-solated nano-sheet Si (Si@CNT/C) has been developed by pyrolysis of the compound of nano-sheet Si and PANI/CNT nanocomposite. The CNT content in the Si@CNT/C/G electrode can be easily controlled by changing the ratio of CNT and PANI in the PANI/CNT nanocomposite. The obtained Si@CNT/C nanocomposite has the excellent conductivity and stress relief caused by silicon volume expansion due to the introduction of CNT as compared to the other literatures.

Experimental

Preparation of Si@CNT/C material

Materials

The ethanol suspension of nano-sheet Si (Si nano-sheet has the feature of 50–200 nm in diameter and 5–10 nm in thickness, silicon content 12.8wt%) was purchased from Jiangsu Xinxiao New Material Technology Co., Ltd. Multi-walled carbon nanotubes (MWCNTs, purity 95–97%, diameter 10–15 nm, length $\leq 10 \mu\text{m}$) were purchased from Tiannai Technology Co., Ltd. CNT/PANI nanocomposite with the CNT and PANI mass ratio of 3:97 and 1:2, respectively, was purchased from Yangzhou Weina Composite Material Technology Co., Ltd. N-methylpyrrolidone (NMP) was purchased from Shanghai Aladdin Bio-Chem Technology Co., Ltd. Polyvinylidene fluoride (PVDF) was purchased from Beijing ARKEMA Co., Ltd. The other chemicals used in this experiment were of analytical grade.

Preparation of Si@CNT/PANI nanocomposite

CNT/PANI nanocomposite powder with the CNT and PANI mass ratio of 3:97 and 1:4 respectively was added to the ethanol suspension of nano-sheet Si, mixed with high-speed dispersion a speed of 1500 r/min for 20 min and further sanded for 2 h. The resulting mixture is under spray drying to obtain Si@CNT/PANI nanocomposite powder.

Preparation of Si@CNT/C/G nanocomposite

Pyrolysis took place in a tubular quartz furnace with nitrogen atmosphere; 5 °C/min of heating rate, pyrolysis temperature of 800 °C maintaining for 1 h, and the resulting pyrolysis products from CNT/PANI with the CNT and PANI mass ratio of 3:97 and 1:4 is Si@CNT(S)/C and Si@CNT(M)/C, respectively.

For the convenience of comparison, fixed the silicon mass fraction of electrode material as 10% and the Si@CNT/C/G electrode with different CNT content can be prepared. The resulting Si@CNT(S)/C/G and Si@CNT(M)/C/G has the mass ratio of Si:CNT:C:G of 10:1.3:25.1:63.6 and 10:10.8:26.7:52.5 respectively.

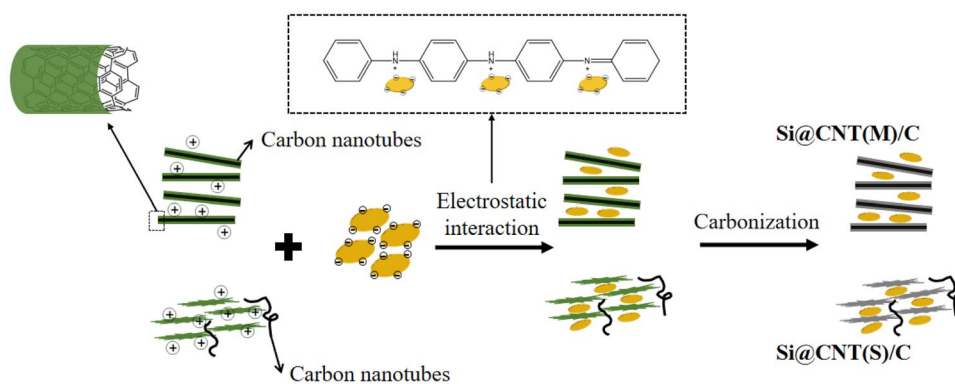
Preparation of the electrodes and coin cells

Weigh the electrode material and binder (PVDF) (weight ratio 9:1), add an appropriate amount of NMP and grind into nanopaste. Coating the above-mentioned nanopaste on copper foil with a thickness of 15 μm and dry. Cut the coated copper foil into circular electrodes with a diameter of 12 mm. The mass loading density of Si@CNT(S)/C/G and Si@CNT(M)/C/G is 1.58 mg/cm² and 0.28 mg/cm² respectively. Dry at 120 °C under vacuum for 24 h to completely vaporize the NMP. The assembly is carried out in a glove box filled with argon (H₂O and O₂ < 0.5 ppm). The electrolyte is a 1 M LiPF₆ solution, and the solvent is a mixed solvent of ethylene carbonate (EC) and dimethyl carbonate (DMC) with a volume ratio of 1:1. The coin-type cells (CR2032) were composed of the fabricated anode materials, the electrolyte, and lithium metal as counter electrode which were separated by Celgard 2325 polypropylene film.

Material characterization

The microstructure and morphology of the samples were investigated by the Field-emission scanning electron microscope (FESEM S-4800II), transmission electron microscope (TEM Tecnai 12), and high-resolution TEM (HRTEM Tecnai G2F30). X-ray photoelectron spectroscopic (XPS) measurements were carried out using ESCALAB 250Xi system. The Brunauer–Emmett–Teller (BET) surface area was analyzed by nitrogen adsorption–desorption isotherms at 77 K in Micromeritics ASAP 2020 system. The N₂ adsorption isotherm was used to determine the pore size distribution via the Barret-Joyner-Halender (BJH) method. X-ray diffraction (XRD) data were collected from 10° to 80° (2 θ angle) in a Bruker AXS D8 ADVANCE X-ray diffractometer using Cu K α radiation (40 kV, 40 mA).

Scheme 1 Schematic diagram of preparation principle of Si@CNT(S)/C and Si@CNT(M)/C



Electrochemical characterization

The galvanostatic charge–discharge (GCD) tests were performed at various current densities within a fixed voltage window of 0.01–3.0 V (vs. Li^+/Li) on Neware battery testing system (CT-4008, Neware, China). Cyclic voltammetry (CV, 0.1 mV s^{-1} , 0.01–3.0 V) measurements and the electrochemical impedance spectroscopy (EIS, 0.01 Hz–100 kHz) tests were performed on CHI660D electrochemical station (Chenhua, Shanghai).

Results and discussion

Preparation of Si@CNT/C nanocomposite

Nano-sheet Si@CNT/PANI is prepared driven by the electrostatic interaction between the nano-sheet Si with negatively charged ions and CNT/PANI nanoparticles with positive charge. When CNT/PANI nanoparticle powder is added into the nano-sheet Si/ethanol suspension, nano-sheet Si@CNT/PANI nanocomposite powder can be formed through sand grinding, filter pressing, and drying. Two different proportions of CNT/PANI (3:97 and 1:4 mass ratio of CNT to PANI) nanoparticles were selected. After carbonization, Si@CNT(S)/C with 2.75wt% and Si@CNT(M)/C with 22.74wt%

of CNT content were obtained accordingly. Scheme 1 shows the preparation principle of Si@CNT/C. Compared with the literature method [18–22], the present process can be easily industrialized.

Figure 1 shows the SEM morphology of CNT/PANI nanocomposite. It can be seen that the CNT/PANI (3:97) nanocomposite presents short fiber morphology with a diameter of 50–60 nm, while the CNT/PANI (1:4) nanocomposite demonstrates the morphology of nanotube morphology with a diameter of 80–100 nm and CNT is completely encapsulated by PANI.

Figure 2 is the TEM image of Si@CNT/PANI nanocomposites. In Fig. 2a, the nano-sheet Si has been dispersed in the CNT/PANI nanocomposites. It can be observed that in Fig. 2b, not only nano-sheet Si has been well dispersed in the CNT/PANI nanocomposites and the carbon nanotubes (marked with a ring) can be clearly seen.

Electrochemical performance of Si@CNT(C)/G nanocomposite

When the silicon content is fixed at 10%, Si@CNT(S)/C/G with 1.3wt% CNT and Si@CNT(M)/C/G with 10.8wt% CNT nanocomposite electrode will be obtained. The X-ray diffraction was carried out to reveal the crystal structure and composition of the Si@CNT(M)/C, which is shown in

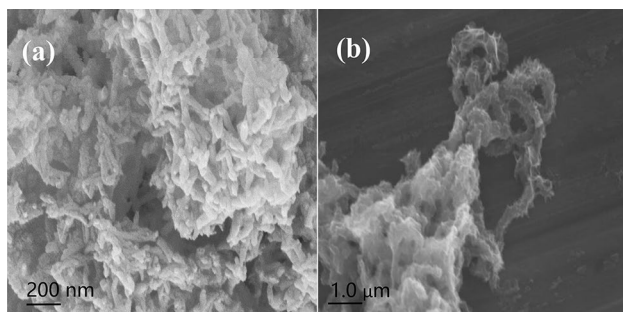


Fig. 1 SEM morphology of CNT/PANI nanoparticles with different mass ratio of CNT to PANI **a** 3:97, **b** 1:4

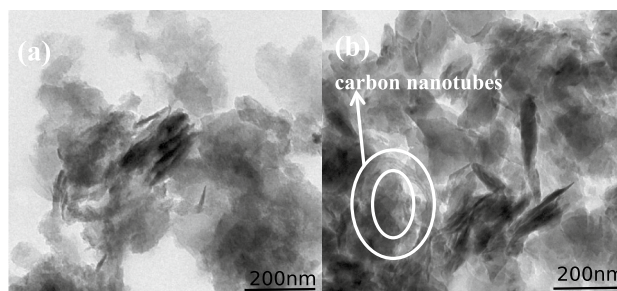


Fig. 2 TEM morphology of Si@CNT/PANI. **a** Si@CNT/PANI (3:97); **b** Si@CNT/PANI (1:4)

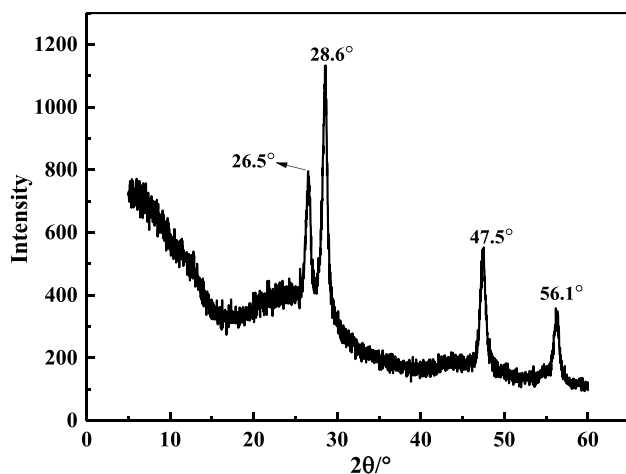


Fig. 3 XRD patterns of Si@CNT(M)/C

Fig. 3. The diffraction peaks at 28.6° (111), 47.5° (220), and 56.1° (311) can be ascribed to the standard XRD data cubic phase Si (JCPDS No.77–2110). Apart from these peaks, an additional peak located at the range of 26.5° is attributed to the (002) reflections of the multi-walled carbon nanotubes. XRD test demonstrates that the CNT has been introduced into nano-sheet Si successfully.

Figure 4 compares the 1st, 2nd, and 3rd discharge/charge profiles of the Si@CNT/C/G anode material between 0.01 and 1.0 V (vs. Li^+/Li). The specific capacity and efficiency of the first cycle of Si@CNT(M)/C/G and Si@CNT(S)/C/G are $1201 \text{ mAh}\cdot\text{g}^{-1}$, 72.4% and $491 \text{ mAh}\cdot\text{g}^{-1}$, 75.8% respectively. The nanocomposite electrode has a different voltage platform has a larger capacity in the first cycle as compared with that in the second cycle, which is caused by the irreversible SEI layer formation. In addition, it can be

seen that the initial capacity of Si@CNT(M)/C/G is much larger than that of Si@CNT(S)/C/G, which is caused by different CNT content in the Si@CNT/C/G and resulting the different specific surface area. The specific surface area of Si@CNT(M)/C is determined to be $46.2 \text{ m}^2/\text{g}$ measured by Brunauer–Emmett–Teller.

Figure 5a compares the cycle diagram at a current density of $100 \text{ mA}\cdot\text{g}^{-1}$ of Si@CNT(S)/C/G and Si@CNT(M)/C/G. The specific capacity and efficiency of the first cycle of Si@CNT(M)/C/G and Si@CNT(S)/C/G are $1201 \text{ mAh}\cdot\text{g}^{-1}$, 72.4% and $491 \text{ mAh}\cdot\text{g}^{-1}$, 75.8% respectively. The initial specific capacity Si@CNT(M)/C/G is more than twice as compared with that of Si@CNT(S)/C/G. The possible reason is the specific surface area difference formed from different CNT network in the Si@CNT/C/G. In the first 80 cycles of Si@CNT(M)/C/G, the specific capacity showed a declining trend until to minimum of $500 \text{ mAh}\cdot\text{g}^{-1}$, after that it gradually increased to $700 \text{ mAh}\cdot\text{g}^{-1}$ and kept until the end of the 500th cycle, while the specific capacity of Si@CNT(S)/C/G is very stable in the first 300 cycles, and then gradually decreases to $200 \text{ mAh}\cdot\text{g}^{-1}$ at the end of the 500th cycle. The $491 \text{ mAh}\cdot\text{g}^{-1}$ of low initial specific capacity suggests that the nano-sheet silicon is not brought into full play, suggesting inadequate electrolyte diffusion channels. The specific capacity can maintain a good retention rate over 300 cycles, which is due to the relatively stable SEI film formed in Si@CNT(S)/C/G electrode. However, after 300 cycles, the specific capacity continues to decline significantly, which suggests the collapse of nano-sheet Si takes place, which leads to reduced conductivity and thus rapid decline of specific capacitance. As for Si@CNT(M)/C/G electrode, the specific capacity declines during the first 80 cycles, which should be caused by the large specific surface area of the Si@CNT(M)/C/G with 10.8wt% CNT. The

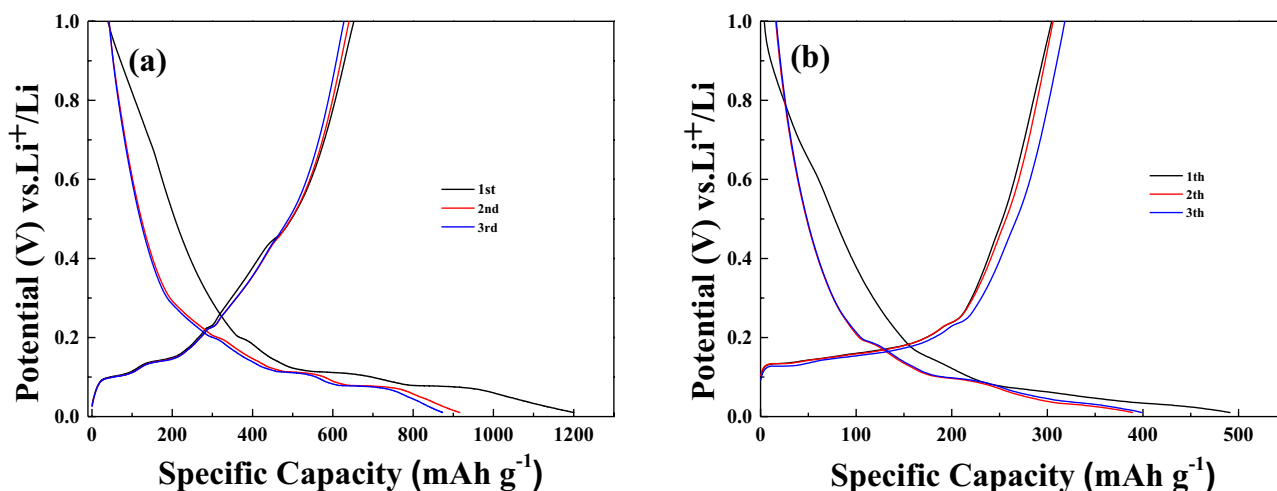


Fig. 4 Charge–discharge voltage profiles of Si@CNT(M)/C/G. **a** Si@CNT(S)/C/G, **b** at a current density of $100 \text{ mA}\cdot\text{g}^{-1}$

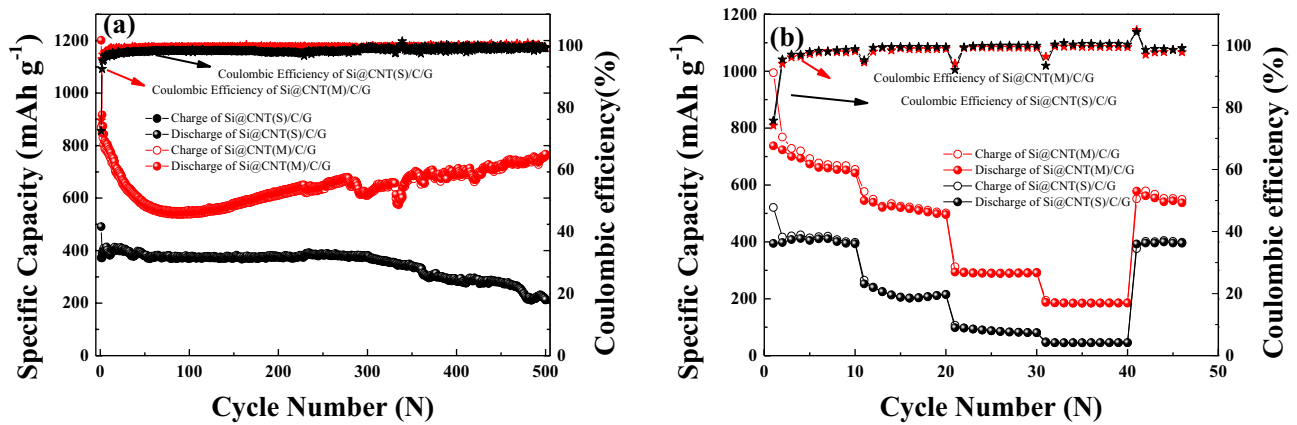


Fig. 5 Comparative cycling performance at a current density of 100 mA·g⁻¹ (a) and cycle rate diagram (b) of Si@CNT(S)/C/G and Si@CNT(M)/C/G

large specific surface area comes into being the more and more SEI film inevitably with the cycle number increases in the initial stage. After that due to the expansion of nano-sheet Si, more active points are released, making the specific capacity gradually rise to 700 mAh·g⁻¹ until the end of the 500th cycle test. As compared Si@CNT(S)/C/G and Si@CNT(M)/C/G electrodes, it is not difficult to infer that Si@CNT(M)/C/G electrode with high content of well uniformly dispersed CNTs can effectively suppressed the huge expansion of nano-sheet Si and maintain the good conductivity during the long-term charge/discharge process.

Figure 5b shows the cycle rate comparison diagram of Si@CNT(S)/C/G and Si@CNT(M)/C/G at current densities of 100 mA·g⁻¹, 500 mA·g⁻¹, 1000 mA·g⁻¹, 2000 mA·g⁻¹, and back to 100 mA·g⁻¹ respectively. Compared with Si@CNT(M)/C/G, Si@CNT(S)/C/G exhibits higher charge–discharge efficiency and excellent rate performance. When the current density is returned from 2000 to 100 mA·g⁻¹, the capacity is

basically restored to its original capacity, with a good capacity retention ability. This difference is also caused by the specific surface area difference of the electrode. Si@CNT(M)/C/G with high specific surface area, within 50 cycles rate test, the stable SEI film has not formed; while Si@CNT(S)/C/G with the low specific surface area, the stable SEI film can be formed. The obtained Si@CNT/C nanocomposite has the excellent initial specific capacity and capacity retention rate as compared to the literature work [23–25], which is due to the unique method to uniformly introduce CNT into Si.

The influence of electrode structure on performance

Electrochemical impedance

In Fig. 6, the diameter of the semicircle in the high frequency zone is related to the contact resistance between the electrolyte and the electrode, and the diameter of the oblate

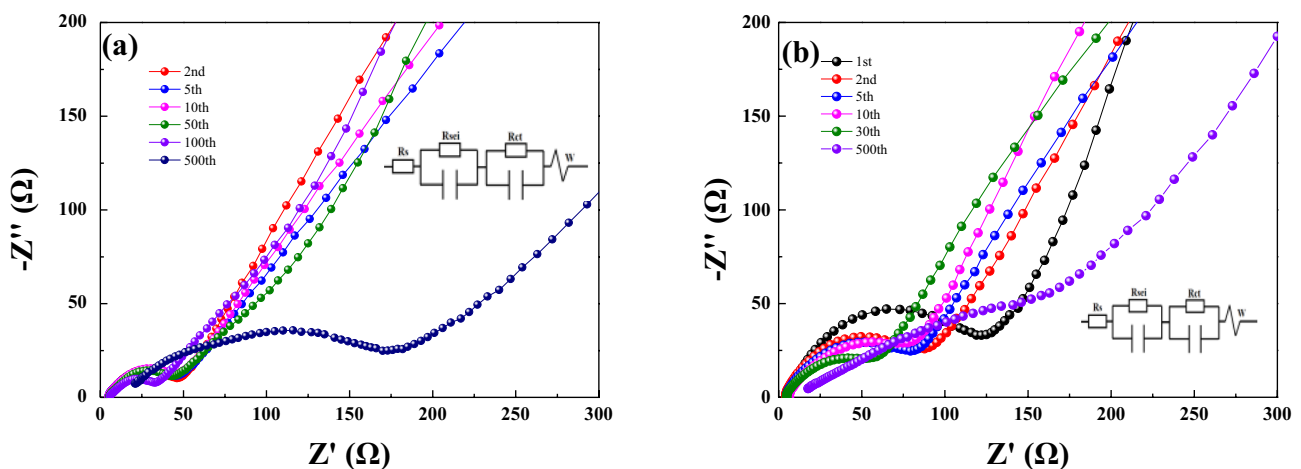


Fig. 6 Electrochemical impedance spectra of a Si@CNT(S)/C/G and b Si@CNT(M)/C/G

Table 1 Electrochemical impedance parameters of Si@CNT(M)/C/G and Si@CNT(S)/C/G

Materials	Si@CNT(M)/C/G (the 2th cycle)	Si@CNT(M)/C/G (the 500th cycle)	Si@CNT(S)/C/G (the 2th cycle)	Si@CNT(S)/C/G (the 100th cycle)	Si@CNT(S)/C/G (the 500th cycle)
Rs/ohm	4.1	19	5.8	5.8	30.5
Rsei/ohm	374	57.9	89.5	3.9	15
Rct/ohm	52.5	21.8	28.1	15.6	64
ω_w /ohm cm ² s ^{-0.5}	911.86	167	246.23	71.03	144.08
D_{Li^+} /cm ² s ⁻¹	3.414×10^{-18}	2.04×10^{-16}	4.683×10^{-17}	1.125×10^{-15}	2.735×10^{-16}

semicircle in the middle frequency zone corresponds to the impedance of the SEI film and the charge transfer impedance between the electrode material and the electrolyte. The oblique line is related to the solid-phase diffusion capacity of lithium ions in the electrode material, and is also called Warburg impedance. In order to obtain the value of the Li⁺ diffusion coefficient (D_{Li^+}) from the electrolyte to the electrode interface, use the following formula:

$$D_{Li^+} = 0.5 \left(\frac{RT}{n^2 F^2 A \sigma_w C} \right)^2 \quad (1)$$

Among them, R corresponds to the gas constant, T corresponds to the absolute temperature, A is the surface area of the electrode, n is the number of transferred electrons, F is Faraday constant, C is the concentration of Li ions, and σ_w is the Warburg factor. Use the equivalent circuit to fit and analyze the impedance spectra, and the results are shown in Table 1. It shows that in the case of Si@CNT(S)/C/G, before 100 cycles, the charge transfer resistance gradually decreases as the number of cycles increases, while D_{Li^+} tends to increase. This result indicates that the initial formation of thin and stable solid electrolyte does not affect the electron transport and is favorable for the diffusion of Li⁺ [26, 27]. However, after the 500th cycle, the R_{ct} of Si@CNT(S)/C/G material increased significantly, while the D_{Li^+} decreased obviously. The results indicate that after a long-term charge/discharge cycles, the internal structure of Si@CNT(S)/C/G material deteriorates due to the structure collapse of the nano-sheet Si and the breakdown of the electron transport passageway compared to that in the beginning of the cycles. In the case of Si@CNT(M)/C/G, it has the SEI film impedance of 374 Ω and charge transfer resistance of 52.5 Ω after the 2th cycle, which is much higher than that of 57.9 Ω and 21.8 Ω and D_{Li^+} is increased by nearly two orders of magnitude after the 500th cycle. The electrochemical impedance spectroscopy analysis indicates that the long-time cycling stability of Si@CNT(M)/C/G is caused by its good conductivity and the adequate ion transport channel. Therefore, it can be safely concluded that Si@CNT(M)/C/G with 10.8wt% of CNT can effectively maintain the stability of the electrode structure, while the Si@CNT(S)/G with 1.3wt% of CNT cannot suppress the huge volume expansion of nano-sheet Si during 500 cycles.

Electrode surface composition analysis

In order to further confirm the change of Si@CNT(S)/C/G electrode microstructure after 500 cycles, Fig. 7 compares the TEM of nanocomposites after the Si@CNT(S)/C/G battery is disassembled and washed with solvent after the 50th cycle and the 500th cycle respectively. It is not hard to see from Fig. 7a that the surface of graphite and nano-sheet Si is very clean without the observable SEI layer after the 50 cycles. Significantly differently, it is obvious to find the dendritic substances in Fig. 7b after 500 cycles. During the charge/discharge process, lithium dendrite is uniformly deposited on the anode surface. Due to kinetic constraints, when the salt concentration on the anode surface decreases, the overpotential increases (0.5–3.5 V/Li), resulting in irregular deposition and the formation of whisker or needle-like dendrites [28]. Dendritic or mossy lithium metal microstructure is formed on the surface of anode electrode, which leads to rapid capacity attenuation [29]. The deposition of lithium dendrites on Si@CNT(S)/C/G after 500 cycles corresponds to the lower diffusion coefficient (2.735×10^{-16}) of Si@CNT(S)/C/G (Table 1), which confirms that Li⁺ moves slower in the skeleton of Si@CNT(S)/C/G after long cycles. This phenomenon of lithium dendrites should be caused by the volume change of Si@CNT(S)/C/G battery between the 300th and 500th cycle. Observe carefully, lots of “spots” can be seen on

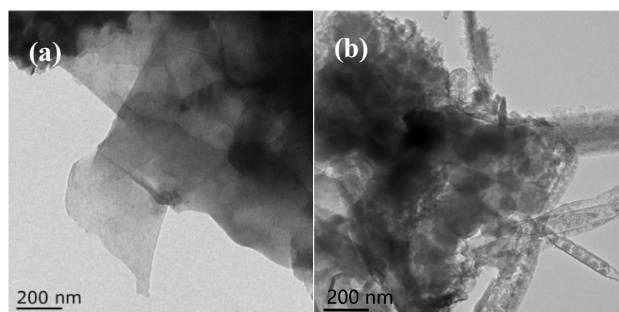


Fig. 7 TEM morphology of Si@CNT(S)/C/G electrode material taken it apart and washed with solvent **a** after 50 cycles and **b** after 500 cycles

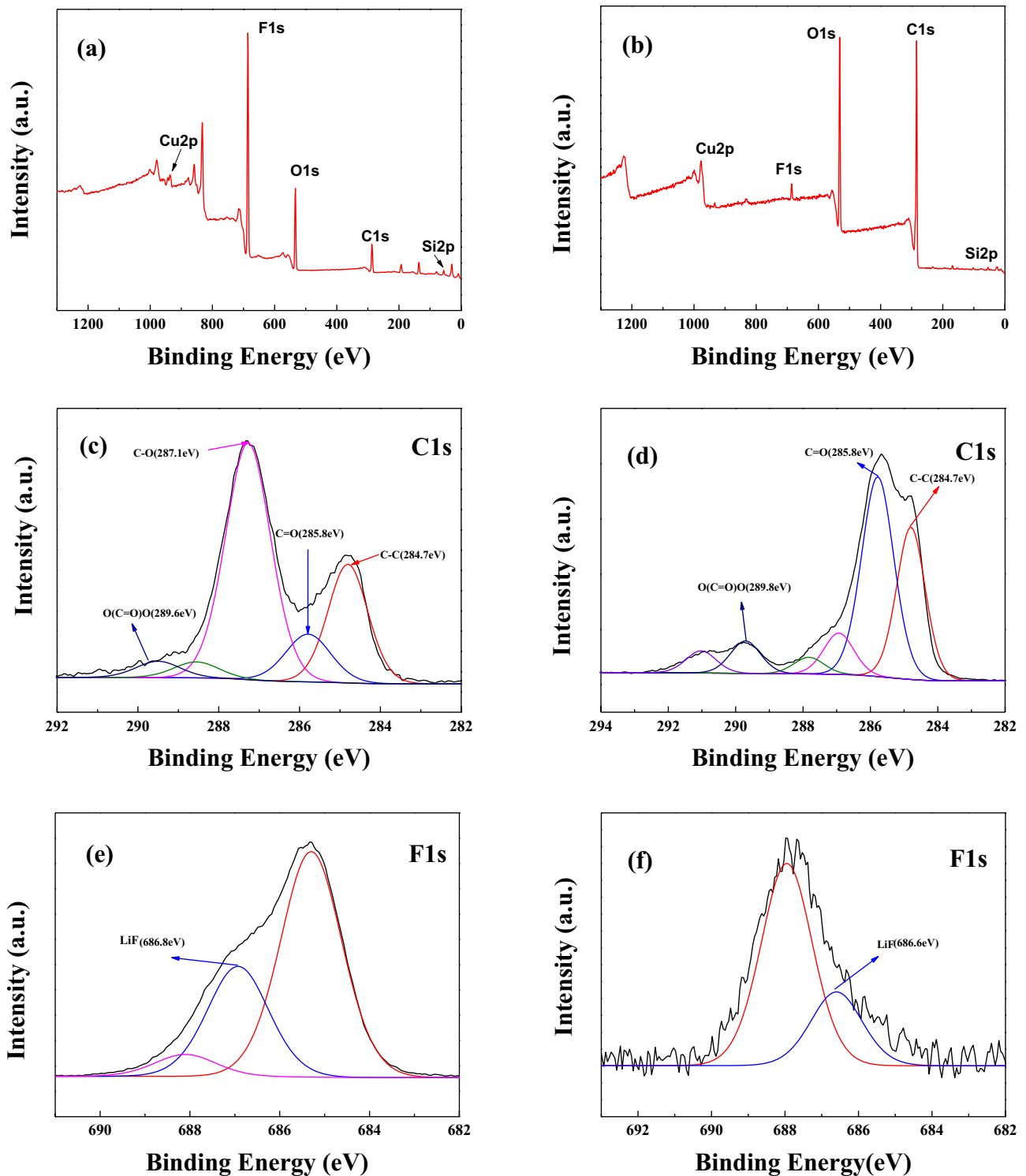


Fig. 8 XPS of Si@CNT(S)/C/G: **a** survey spectrum, **c** C1s spectrum, **e** F1s spectrum after 50 cycles; **b** survey spectrum, **d** C1s spectrum, **f** F1s spectrum after 500 cycles

the surface of lithium dendrite, which is in the rechargeable lithium battery. At the same time, the dendrite solid electrolyte film formed by lithium ions in the electrolyte increases the surface area of the anode and induces the

rupture and reconstruction of the solid electrolyte film, which accelerates the excessive consumption of electrolyte and the formation of dead metal, thus accelerating the deterioration of battery performance.

XPS analysis provides another effective method to reveal the causes of Si@CNT(S)/C/G deterioration. Figure 8 shows the nanocomposites after the Si@CNT(S)/C/G battery is disassembled and washed with solvent after 50 cycles and 500 cycles respectively. Figure 8a and b, the survey XPS spectra demonstrate the presence of carbon (C1s), oxygen (O1s), fluorine (F1s), and low intensity silicon (Si2p) peaks. Figure 8c is a spectra of C1s, with one of the strongest peaks at 287.1 eV and three weakest peaks at 289.6 eV, 285.8 eV, and 284.7 eV, correspond to the C–O, O–C=O–O, C=O, and C–C groups of graphite respectively [30]. The C–C peak is derived from the carbon electrode, and the C–O peak indicates that there are some special surface functional groups on the carbon surface. The peak area ratio of O–C=O–O after 50 cycles (Fig. 8c) is significantly smaller than 500 cycles (Fig. 8d), which means that the SEI on the surface after 50 cycles is thinner than that of the after 500 cycles [30]. The “C” atomic content becomes 63.24% after the 50th cycle, suggesting that there is a new carbon surface appeared. Comparing Fig. 8e and f, it is found that the characteristic F1s peak significantly weakens after 500 cycles in comparison with that after 50 cycles confirmed by the “F” atomic content decreases from 34.94 to 1.64%. Only the weak F1s peak at 687 eV, which is assigned to LiF, appears on the spectrum after 500 cycles, confirming that electrolytes are depleted.

Conclusions

Nanocarbon-isolated nano-sheet Si with different CNT content has been successfully constructed through carbonization of the compound of nano-sheet Si and CNT/PANI nanocomposite. The results show that Si@CNT(M)/C/G with high (10.8wt%) CNT content has higher initial specific capacity (1201 mAh·g⁻¹) and the much high capacity retention (83.68%) during 500 cycles as compared with those (491.5 mAh·g⁻¹ of initial specific capacity, 54.85% of capacity retention) for Si@CNT(S)/C/G with low (1.3wt%) CNT content. The uniformly distributed CNT in the Si@CNT(M)/C/G electrode demonstrates the effective to minimize mechanical strain and cracking of nano-sheet Si and maintaining the good conductivity. The preparation method of CNT introduced into Si/C electrode uniformly in industrial scale provides an effective strategy to solve the current dilemma.

Funding This research was financially supported by Industrial Prospect and Key Core Technology Projects of Jiangsu Province (SBE2019030778) and Science and Technology Cooperation Funds of Yangzhou City and Yangzhou University (YZ2020179).

References

- Peng LA, Hk A, Stm B et al (2020) Diverting exploration of silicon anode into practical way: a review focused on silicon-graphite composite for lithium ion batteries. *Energy Storage Mater.* <https://doi.org/10.1016/j.ensm.2020.11.028>
- Sun YK, Myung ST, Park BC et al (2009) High-energy cathode material for long-life and safe lithium batteries. *Nat Mater* 8(4):320. <https://doi.org/10.1038/nmat2418>
- Kwak WJ, Rosy Sharon D et al (2020) Lithium–oxygen batteries and related systems: potential, status, and future. *Chem Rev.* <https://doi.org/10.1021/acs.chemrev.9b00609>
- Wiggers H, Sehlleier YH, Kunze F et al (2020) Self-assembled nano-sheet Si/graphite hybrid embedded in a conductive polyaniline matrix for the performance enhancement of industrial applicable lithium-ion battery anodes. *Solid State Ion* 344:115117. <https://doi.org/10.1016/j.ssi.2019.115117>
- Tarascon JM, Armand M (2010) Issues and challenges facing rechargeable lithium batteries. *Nature.* https://doi.org/10.1142/9789814317665_0024
- Bell CG, Fei G, Wei Y et al (2018) Obligatory and facilitative allelic variation in the DNA methylome within common disease-associated loci. *Nat Commun* 9(1):8. <https://doi.org/10.1038/s41467-017-01586-1>
- Pellegrini V, Bodoardo S, Brandell D et al (2019) Challenges and perspectives for new material solutions in batteries *Solid State Commun* 303–304:113733. <https://doi.org/10.1016/j.ssc.2019.113733>
- Jin, Yan, Zhu et al (2017) Challenges and recent progress in the development of si anodes for lithium-ion battery. *Adv Energy Mater.* <https://doi.org/10.1002/aenm.201700715>
- Gonzalez AF, Yang NH, Liu RS (2017) Silicon anode design for lithium-ion batteries: progress and perspectives. *J Phys Chem C* *acs.jpcc.7b07793*. <https://doi.org/10.1021/acs.jpcc.7b07793>
- Tao W, Wang P, You Y et al (2019) Strategies for improving the storage performance of silicon-based anodes in lithium-ion batteries. *Nan Mi Yan Jiu* 12(8):11. <https://doi.org/10.1007/s12274-019-2361-4>
- Wang F, Song C, Zhao B et al (2020) One-pot solution synthesis of carbon-coated silicon nanoparticles as an anode material for lithium-ion batteries. *Chem Commun* 56. <https://doi.org/10.1039/C9CC07255A>
- Yin YX, Wan LJ, Guo YG (2012) Silicon-based nanomaterials for lithium-ion batteries. *Ke Xue Tong Bao* 57(32):7. <https://doi.org/10.1007/s11434-012-5017-2>
- Lee JH, Kim WJ, Kim JY et al (2008) Spherical silicon/graphite/carbon composites as anode material for lithium-ion batteries. *J Power Sourc* 176(1):353–358. <https://doi.org/10.1016/j.jpowsour.2007.09.119>
- Huang S, Cheong LZ, Wang D et al (2017) Nanostructured phosphorus doped silicon/graphite composite as anode for high-performance lithium-ion batteries. *ACS Appl Mater Interfaces* 23672. <https://doi.org/10.1021/acsami.7b04361>
- Su M, Wang Z, Guo H et al (2014) Enhancement of the Cyclability of a Si/Graphite@Graphene composite as anode for Lithium-ion batteries. *Electrochim Acta* 116:230–236. <https://doi.org/10.1016/j.electacta.2013.10.195>
- Seo J-S, Yoon S-H, Na B-K (2021) Electrochemical characteristics of Si/SiO₂/C anode material for lithium-ion battery according to addition of CNT and CNF Compounds. *Korean Chem Eng Res* 59(1):35–41. <https://doi.org/10.9713/kcer.2021.59.1.35>
- Ashuri M, He Q, Shaw LL (2015) Silicon as a potential anode material for Li-ion batteries: where size, geometry and structure matter. *Nanoscale* 8(1):74–103. <https://doi.org/10.1039/C5NR05116A>

18. Kim SO, Manthiram A (2015) A facile, low-cost synthesis of high-performance silicon-based composite anodes with high tap density for lithium-ion batteries. *J Mater Chem A* 3:2399–2406. <https://doi.org/10.1039/C4TA06113F>
19. Sultana I, Rahman MM, Mateti S et al (2017) K-ion and Na-ion storage performances of $\text{Co}_3\text{O}_4\text{-Fe}_2\text{O}_3$ nanoparticle-decorated super P carbon black prepared by a ball milling process. *Nanoscale* 9. <https://doi.org/10.1039/C6NR09613A>
20. Xu J, Jeon IY, Seo JM et al (2014) Edge-selectively halogenated graphene nanoplatelets (XGnPs, X = Cl, Br, or I) prepared by ball-milling and used as anode materials for lithium-ion batteries. *Adv Mater* 26(43):7317–7323. <https://doi.org/10.1002/adma.201402987>
21. An W, Gao B, Mei S et al (2019) Scalable synthesis of ant-nest-like bulk porous silicon for high-performance lithium-ion battery anodes. *Nat Commun* 10(1). <https://doi.org/10.1038/s41467-019-09510-5>
22. Liu W, Xu H, Qin H et al (2020) Rapid coating of asphalt to prepare carbon-encapsulated composites of nano-sheet Si and graphite for lithium battery anodes. *J Mater Sci* 55(10):4382–4394. <https://doi.org/10.1007/s10853-019-04313-x>
23. Shuaifeng L, Cheng X, Zhao Y et al (2014) Superior performance of ordered macroporous TiNb_2O_7 anodes for lithium ion batteries: understanding from the structural and pseudocapacitive insights on achieving high rate capability. *Nano Energy*. <https://doi.org/10.1016/j.nanoen.2017.01.058>
24. Wan X, Mu T, Shen B et al (2022) Stable silicon anodes realized by multifunctional dynamic cross-linking structure with self-healing chemistry and enhanced ionic conductivity for lithium-ion batteries. *Nano Energy*. <https://doi.org/10.1016/j.nanoen.2022.107334>
25. Shin M-S, Lee T-M, Lee S-M et al (2019) Electrochemical properties of micro sized Silicon / CNT / carbon composite particles as cathode active materials for lithium secondary batteries. *J Electric* 22(3):112–121. <https://doi.org/10.5229/JKES.2019.22.3.112>
26. Zhao Q, Stalin S, Archer LA (2021) Stabilizing metal battery anodes through the design of solid electrolyte interphases. *Joule* 5(5):1119–1142. <https://doi.org/10.1016/j.joule.2021.03.024>
27. Chen Y, Huang H, Liu L, Chen, Y Han Y (2021) Diffusion enhancement to stabilize solid electrolyte interphase. *Adv Energy Mater* 11(40). <https://doi.org/10.1002/aenm.202101774>
28. Mka A, Yn A, Th B et al (2021) How to avoid dendrite formation in metal batteries: Innovative strategies for dendrite suppression. *Nano Energy* 86. <https://doi.org/10.1016/j.nanoen.2021.106142>
29. Li W, Kim UH, Dolocan A et al (2017) Formation and inhibition of metallic lithium microstructures in lithium batteries driven by chemical crossover. *ACS Nano* 5853. <https://doi.org/10.1021/acs.nano.7b01494>
30. Yang Y, Lu Z, Xia J et al (2020) Crystalline and amorphous carbon double-modified silicon anode: towards large-scale production and superior lithium storage performance. *Chem Eng Sci* 116054. <https://doi.org/10.1016/j.ces.2020.116054>

Publisher's Note Springer Nature remains neutral with regard to jurisdictional claims in published maps and institutional affiliations.

Springer Nature or its licensor holds exclusive rights to this article under a publishing agreement with the author(s) or other rightsholder(s); author self-archiving of the accepted manuscript version of this article is solely governed by the terms of such publishing agreement and applicable law.